Two-dimensional model of flow and transport in porous media: linking heterogeneous anisotropy with stratal patterns in meandering tidal channel deposits of the Venice Lagoon (Italy)

Elena Bachini[a], Elena Bellizia[b], Mario Putti[c], Andrea D'Alpaos[b] and Massimiliano Ghinassi[b]

[a]*Institute of Scientific Computing, TU Dresden, Germany*
[b]*Department of Geosciences, University of Padua, Italy*
[c]*Department of Mathematics "Tullio Levi-Civita", University of Padua, Italy*

ARTICLE INFO

Keywords:
Meandering tidal channel deposits
Heterogeneous anisotropic conductivity
Groundwater flow and transport

ABSTRACT

Understanding the internal structure of permeable and impermeable sediments (e.g. point-bars and tidal-flat deposits) generated by the evolution of meandering tidal channels is essential for accurate modeling of groundwater flow and contaminant transport in coastal areas. The detailed reconstruction of stratal geometry and hydraulic properties from measurements must be accompanied by depositional history information. In this work, we use high resolution reconstructions of ancient tidal channels of the Venice Lagoon (Italy) to drive 2D simulations of groundwater flow and transport, showing the importance of incorporating information on the sediment accumulation processes into the hydraulic characteristics and how horizontal anisotropy emerging from these processes significantly influences transport. Effective hydraulic conductivity is modeled with a heterogeneous 2D anisotropic tensor with principal directions aligned with observed sedimentation sequences. Comparison of flow and solute dynamics simulated using reconstructed and theoretical hydraulic properties show drastically different pathways of solute propagation.

1. Introduction

Coastal plains are delicate environments where continental and marine processes have intertwined during the past millennia. Holocene fluvial and tidal channels mainly contributed to shaping actual landscapes through the accumulation of complex sedimentary sand bodies (Allen, 1965; Bridge, 2003; Khan et al., 1997). The overall flat topography and the availability of freshwater from surficial aquifers make coastal areas suitable for urbanization, agricultural and industrial activities (Amorosi et al., 2013; Boyer et al., 2006; Delagnes et al., 2012). On the other hand, agriculture has to interface with saltwater intrusion, which endangers the soil productivity (Da Lio et al., 2015; Nofal et al., 2015), and industrial activities are often responsible to pollutant dispersion in the groundwater (Carraro et al., 2015; Desbarats et al., 2014). Pollutant propagation (e.g., fuel dispersion, herbicides, chemical contamination) is a crucial environmental problem that has been investigated under multidisciplinary approaches (Benner et al., 2008; Carraro et al., 2015, 2013; Christensen and Hatfield, 1994; Desbarats et al., 2014; Harvey et al., 2006; Hatfield and Christensen, 1994; Şimşek et al., 2008; Yang et al., 2001). In coastal areas, the groundwater flow is driven by preferential pathways within permeable deposits accumulated by ancient fluvial and tidal channels. For these reasons, understanding the internal structure of these deposits (i.e., porous media) and flow motion

* elena.bachini@tu-dresden.de

within them is essential to manage unwanted and threatening phenomena such as saltwater intrusion and pollutant propagation. In lagoonal environments, the sedimentary elements associated with the evolution of meandering tidal channels includes in-channel and overbank deposits. In-channel elements are sand-prone bars (i.e., point bars) and mud-rich channel fills, which are accumulated during channel migration and deactivation, respectively. Overbank deposits (e.g., tidal flats) are mainly muddy, and along with channel fill units, are the less permeable elements forming coastal sedimentary successions (Cosma et al., 2020a).

Flow and transport processes in porous media can be quantitatively estimated by means of numerical models approximating the solution of the relevant partial differential equations. Solute transport is driven by the fluid velocity as calculated from the solution of the flow equation. A three-step procedure is used: i) solve the flow equation and determine the distribution of the hydraulic head; ii) calculate the discrete velocity vector field from the gradient of the hydraulic potential; and, iii) solve the solute transport equation. The velocity field, which is governed by Darcy law, depends crucially on the hydraulic conductivity coefficient, the mathematical object encoding the internal structure of the geologic formation. This coefficient is typically defined at a spatial scale that is sufficiently large for proper homogenization but small enough to distinguish different geologic formations. The nature of groundwater flow and transport is such that the structure and spatial variability of the conductivity tensor affect the hydraulic head and its gradient at different scales. Indeed, while the hydraulic head is characterized by a global scale of variability (geometric dimension of the geologic formation), its gradient varies at a scale of the order of the scale at which the hydraulic conductivity has been characterized. Solute transport is determined by the flow velocity and direction, and thus acts at the latter scale. The accuracy with which solute fate is predicted is intrinsically determined by the accuracy of Darcy velocity $\mathbf{q}$. The detailed reconstruction of both the order of magnitude of the elements of the hydraulic conductivity tensor and the principal directions of anisotropy is crucial for precise quantitative estimates of solute transport. Pauloo et al. (2021). It is well known that, in complex and vertically expanded sedimentary successions (e.g. (Ghinassi et al., 2013)), anisotropy originates from the averaging of mostly vertical hetereogeneities (Renard and de Marsily, 1997) caused by the prevalently one dimensional sedimentation process. On the other hand, horizontal anisotropy is negligible in groundwater simulations and it is embodied by the structural heterogeneity attributed to hydraulic conductivity (Fogg et al., 1998, 2000; Weissmann et al., 2004). However, there are many instances when horizontal anisotropy can play a role, but these are only seldom investigated and mostly in non-sedimentary formations Purkis and Vlaswinkel (2012). One of the contributions of this paper is to show how an accurate characterization of horizontal anisotropy based on interpretation of the depositional processes can lead to drastically different effects with respect to the case where simplistic depositional models are considered. The presence of strong anisotropies in the horizontal plane add to the difficulties arising from the classical vertical anisotropy and require accurate and anisotropy-robust numerical solvers. In summary, a reliable geologic model should consider detailed reconstructions of stratal geometries and sediment properties. The former can be obtained by coupling geophysical techniques with local drilling. Information from samples obtained from drilling can be used to estimates the order of magnitude of the conductivity coefficients. However, this information does not provide clues on the direction of anisotropy, which must be determined by studying the depositional history of the sediments.

The present work investigates modes of 2D flow within deposits of an ancient tidal channel of the Venice Lagoon (Italy) using numerical models of flow and transport accompanied by a high resolution characterization of stratal geometries (Bellizia et al., 2022), spatial distribution of sediment properties, and reconstruction of anisotropy directions. A detailed geological description is less important in areas filled with fine sediments where no flow of practical interest occurs, and so our focus is mainly concentrated on the tidal channel. The objective of this study are to show via numerical experiments the importance of the characterization described above and of the robustness of the numerical discretization used to resolve the inherent spatial variability of the coefficients. To this aim, we use linear finite element method for

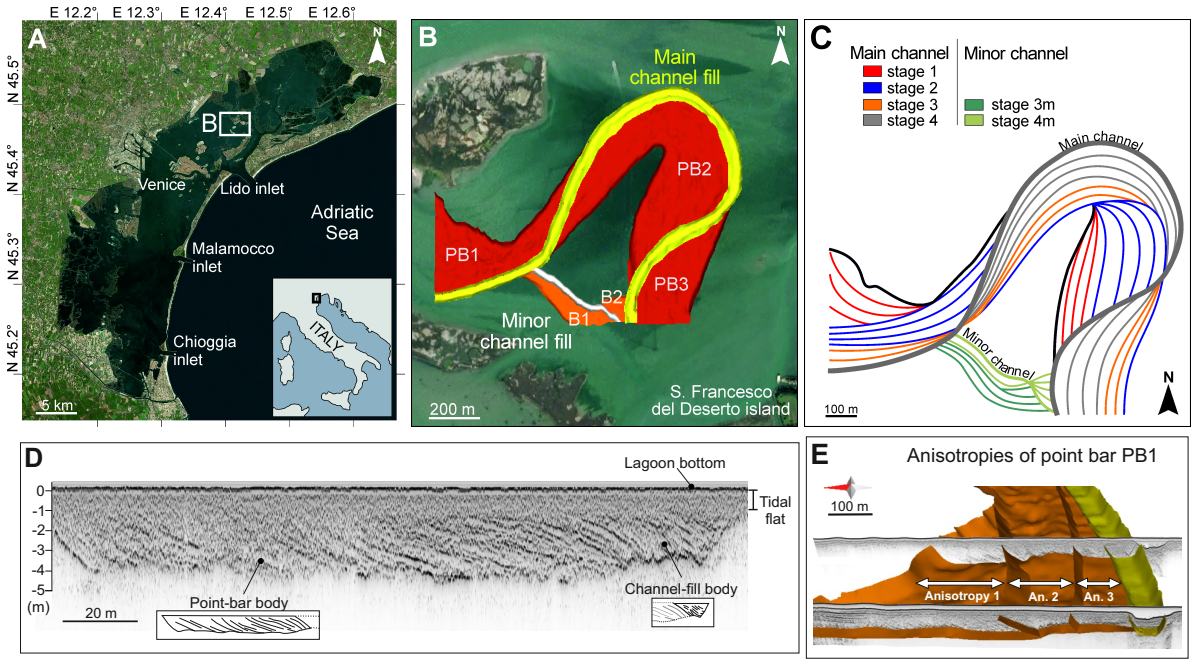

Figure 1: The prototype case. (A) Geographic position of the study area in the Venice Lagoon. (B) Position of the buried meandering channel in the study area: the main channel fill (in yellow) with associated point bars (in red), and the minor channel fill (in white) with the bank-attached bars (in orange). (C) The four morphodynamic stages of the study channel. (D) Example of a seismic section of the area, showing morphologies of the lagoon bottom, tidal flat and paleo-channel bodies. (E) Partial 3D view of point bar PB1 with accretionary boundaries defining the internal anisotropies.

spatial discretization because of its robustness against mesh locking when strong anisotropy ratios are present (Manzini and Putti, 2007; Mazzia et al., 2011) together with an efficient conjugate gradient method with ad-hoc preconditioning. We recall here that mesh locking is a numerical phenomenon by which the numerical solver becomes inaccurate if the mesh is not fine enough The aim is to highlight a prototypical test case that can be used as starting point for larger scale studies, addressing for example management of aquifers in coastal areas in terms of propagation of pollutants or saltwater intrusion.

Results from this work can be applied to worldwide studies of flow motion within surficial permeable bodies originated by evolution of tidal meandering channels, especially for those developed in coastal areas affected by a microtidal regime.

2. The prototype case: buried meandering tidal channel deposits of the Venice Lagoon

The prototype case deposits are placed in the northern sector of the Venice Lagoon (NE Italy) (fig. 1 A), which is the largest brackish water body of the Mediterranean basin, developed over the last 6000 years during Holocene transgression, and currently covers an area of about 550 km^2 (Zecchin et al., 2009, 2008). The Venice Lagoon is affected by a semi-diurnal micro-tidal regime, with an average tidal range of ca. 1 m (D'Alpaos et al., 2013) and is dissected by a dense network of tidal channels, which cut through both tidal flats and salt marshes (Finotello et al., 2019, 2020; Ghinassi et al., 2018a,b).

The prototype case deposits are buried below 1 m of tidal-flat deposits located close to the S. Francesco del Deserto island, where water depth is ca. 1 m. These deposits were formed in the late Holocene by a 35 m-wide paleochannel (Madricardo et al., 2007) and consist of three adjacent point-bar bodies, named PB1,

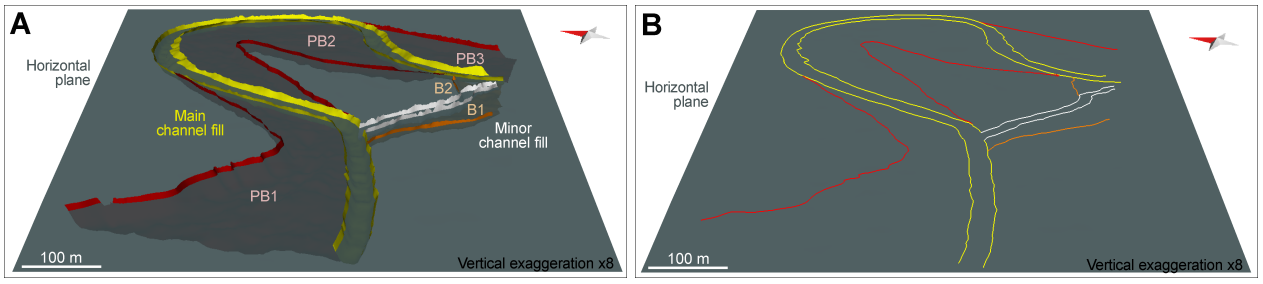

Figure 2: 3D basal surfaces of the studied depositional elements (i.e., channel fills and channel bars) intersected with a horizontal plain (A), to obtain the 2D intersection lines (B) that have been used to defined the 2D polygons for flow and transport simulations.

PB2 and PB3 which are on average 2.5 m thick (Bellizia et al., 2022). The channel belt axis of the paleo-channel system is WNW-ESE oriented (fig. 1 B). A minor channel, ca. 20 m wide and trending WNW-ESE, crossed bar PB2 developing two bank-attached bars, named B1 and B2. Sedimentary cores show that bar deposits mainly consist of laminated silt and very fine sand with 0.5 - 1 mm-thick muddy laminae. Channel fill and over-bank deposits are made of homogeneous mud (Madricardo et al., 2007; Bellizia et al., 2022). A detailed 3D model based on seismic data (Bellizia et al., 2022) allowed us to depict the effective geometry of bar bodies and to identify four major evolutive stages of the study channel. Reconstructed geometry of bars shows that they started to accrete from a sinuous channel, as clearly shown by the arcuate shape of bar PB1, which encloses homogeneous over-bank mud (fig. 1 C). During the major evolutive stages, bars PB1-3 grew in different directions accumulating silty layers on their slope. These layers strike and dip in different directions, creating anisotropies within the bar sedimentary bodies (fig. 1 E).

3. Methods

The main aim of this work is to show that anisotropy in the hydraulic conductivity tensor plays a major role in the movement of contaminants, such as nutrients and other substances infiltrated from the surface and saltwater intruding from the sea. To drive our experiments, we use a detailed reconstruction of the complex formation described above together with an in depth understanding of the sedimentary processes that formed it. Another objective is to highlight the challenging issues emerging from the numerical simulations under strong anisotropic flows. To this aim, we design different boundary conditions that trigger numerical ill-conditioning while maintaining the realistic behavior of the test case. The design of our numerical experiments is geared towards these objectives.

3.1. From geological reconstruction to model input data

Typical models of groundwater flow and transport at the regional scale consider a two-dimensional vertically averaged framework (de Marsily, 1986). This assumption is grounded on the consideration that the vertical flux is small with respect to its horizontal component. The 2D approach is warranted when infiltration from the surface can be neglected. Within this framework, paleo-river beds act as preferential pathways for the movement of contaminants, since they tend to form permeable, elongated sedimentary bodies which are laterally and vertically confined (Gibling, 2006). In Holocene sedimentary bodies, which are not deformed and show a spatial distribution that reflects the present-day orographic configuration, the morphology and hydraulic characteristics of these formations as well as the regional gradient forcing the flow are the main drivers that need to be taken into account in the design of our test cases. The 2D model for the proposed simulation has been obtained from a detailed 3D reconstruction arising from the integration of seismic data and sedimentary core data. This process allows one to define the boundaries between different

types of deposits (e.g., bar, channel fill and overbank deposits). Laminated silt and very fine sand forming bar deposits show a different spatial orientation, which arises from the lateral shifting of the study channel during the four main stages of bar evolution (fig. 1 C). Silty levels represent the major permeability barriers within bar deposits, and their orientation is consistent with that of the layers generated during the four growth stages.

A total of 201 high resolution (decimeter-scale) seismic sections were used to correlate surfaces bounding the major depositional units in a 3D space. Sedimentary cores were used to integrate such a reconstruction and to define the spatial distribution of different types of deposits. Starting from this three-dimensional reconstruction, we define the average planar position of the morphological features forming our tidal deposits, namely the channels (i.e., main channel and minor channel), the bars (i.e., PB1, PB2, PB3 of the main channel, and B1, B2 of the minor one), and the surrounding subtidal platform. This is obtained by intersecting the mesh surfaces forming the 3D model with a horizontal plane that cuts the reconstructed bar at the half of the thickness (fig. 2 A). The resulting intersection lines are used to define polygons, which define boundaries of different types of deposits (i.e., overbank, bar and channel fill) in a 2D horizontal domain (fig. 2 B). Within bar deposits, the same approach is been used to detect boundaries between deposits accreted during the four depositional phases (fig. 1 C). Additionally, seismic data indicate the orientation of layers within these deposits, pointing out also the alignment of the major permeability barriers. Specifically, in the obtained 2D model, conductivity is considered to reach its maximum and minimum in directions parallel and orthogonal to the muddy laminae, respectively. The muddy nature of overbank and channel-fill deposits allows one to ascribe them an isotropic conductivity of 10^{-8} m/s. In bar deposits, a conductivity of 10^{-6} m/s and 10^{-8} m/s is assigned in the directions parallel and orthogonal to muddy laminae, respectively.

3.2. Mathematical models of flow and transport

The mathematical model considers a flow equation, to determine the flux vectors of the flow in the porous media, and successively a transport equation to simulate the transport of contaminants due to the computed fluxes. The flow equation is characterized by the presence of spatially varying anisotropy. The idea is to relate the spatial distributions of the anisotropy to the sediment forming depositional environment and test the possible influence of heterogeneous anisotropy on the groundwater flow and transport.

Flow equation. The flow equation in a confined aquifer in $\mathbb{R}^3$ reads:

$$S_s \frac{\partial h}{\partial t} - \nabla \cdot \left(\mathbb{K}_s \nabla h \right) = f \,, \tag{1}$$

where S_s [1/L] is the elastic storage coefficient, $\mathbb{K}_s$ [L/T] is the hydraulic conductivity tensor, and f [1/T] is the (external) source term. The scalar function h [L] is the unknown variable and represents the hydraulic head. We couple this equation with Dirichlet boundary conditions. Darcy flux is then computed by $\mathbf{q} = -\mathbb{K}_s \nabla h$ [L/T]. We will use equivalently the words Darcy flux or Darcy velocity or simply velocity to mean specific discharge (see (Haitjema and Anderson, 2016) for a discussion on the difference between Darcy velocity and pore velocity). In our simplified two-dimensional framework, we assume that the confined aquifer has a unitary thickness b [L]. Thus, the above equation can be written in a two-dimensional domain Ω, coinciding with a planar shape of the geologic formation, with the hydraulic conductivity replaced by the hydraulic transmissivity $\mathbf{T} = \mathbb{K}_s b$ [L^2/T] and the elastic storage coefficient replaced by the storativity coefficient $S = S_s b$ [-]. These simplistic assumptions are dictated by the lack of data in the fully three-dimensional distribution of hydraulic properties. We realize that a fully 3D framework would be much more appropriate and it will be tackled as soon as enough data are collected. However, a 3D approach would need to solve first the formidable task of assessing permeability anisotropy as it relates to the complex sedimentary process in a meandering morphometry.

Since we are interested in a steady-state flow ($\partial h/\partial t = 0$) with $f = 0$ in the presence of anisotropy, the equation simplifies to:

$$\nabla \cdot (-\mathbf{T} \nabla h) = 0 \qquad \text{in } \Omega \tag{2}$$

$$h = h_D \qquad \text{on } \partial\Omega \tag{3}$$

where $\mathbb{K}_s$ is the 2×2 symmetric tensor varying in space that embodies the anisotropic behavior, and h_D is a prescribed value of the solution at the boundary. If the diffusion process is isotropic the conductivity tensor is defined by $\mathbb{K}_s = \kappa\mathbb{I}$, where κ is a scalar value and $\mathbb{I}$ the identity matrix. In the anisotropic case, the tensor is no longer diagonal. We have to define the two vectors $\mathbf{v}$, $\mathbf{w}$ that provide the principal directions of anisotropy (i.e. the eigenvectors of $\mathbb{K}_s$), together with two compatible conductivity values (i.e., the corresponding eigenvalues). Then, the final anisotropic tensor is defined by:

$$\mathbb{K}_s = U \Lambda U^T = \begin{bmatrix} v_1 & w_1 \\ v_2 & w_2 \end{bmatrix} \begin{bmatrix} \kappa_1 & 0 \\ 0 & \kappa_2 \end{bmatrix} \begin{bmatrix} v_1 & v_2 \\ w_1 & w_2 \end{bmatrix}$$

In practice, we set the first eigenvalue κ_1 as the coefficient κ given by the material with the corresponding eigenvector $\mathbf{v}$, the preferential direction of the process. Then, the vector $\mathbf{w}$ is defined to be orthogonal to $\mathbf{v}$ and the second eigenvalue κ_2 is set to be $\kappa_2 = \kappa_1 * r_a$, where r_a is the chosen anisotropy ratio.

Transport equation. The transport of contaminants in a certain domain Ω is governed by the following equation:

$$n\frac{\partial c}{\partial t} = \nabla \cdot (\mathbb{D} \nabla c) - \nabla \cdot (\mathbf{q}\, c)\ , \tag{4}$$

where n [-] is the porosity and we consider in the first order term the velocity field given by Darcy flux $\mathbf{q}$ [L/T] as computed by the flow equation. In this case c [-] is the normalized (mass/mass) concentration of the contaminant, and $\mathbb{D}$ [L^2/T] is the dispersion tensor (Bear, 1979), defined as:

$$\mathbb{D} = \alpha_L\, |\mathbf{q}|\, \mathbb{I} + \left|\alpha_L - \alpha_T\right| \frac{\mathbf{q}\mathbf{q}^{\mathrm{T}}}{|\mathbf{q}|} + nD_m\mathbb{I}\,, \tag{5}$$

where α_L [L] is the longitudinal dispersivity, α_T [L] is the transversal dispersivity and D_m [L^2/T] is the molecular diffusion. The equation can be formed by multiple components if multiple contaminants need to be studied. The mathematical model is completed by Dirichlet/Neumann/Cauchy boundary conditions and by initial conditions.

Numerical solution. The above equations are solved using the CATHY solver (Camporese et al., 2010; Weill et al., 2011), a hydrological model based on linear finite elements with stabilization and preconditioned conjugate gradient (PCG) linear solver. This code has been extensively used in several projects (see for example (Passadore et al., 2012; Scudeler et al., 2016a)) and has been benchmarked against other similar solvers in (Maxwell et al., 2014; Kollet et al., 2017). The presence of strong anisotropic diffusion may cause numerical difficulties depending on the method used in the discretization (Manzini and Putti, 2007). The CATHY solver is capable of tackling demanding applications and also the most extreme anisotropic behavior (Mazzia et al., 2011). The PCG scheme of CATHY has been complemented with ad-hoc preconditioners to handle the severe ill-conditioning arising from the anisotropy ratios.

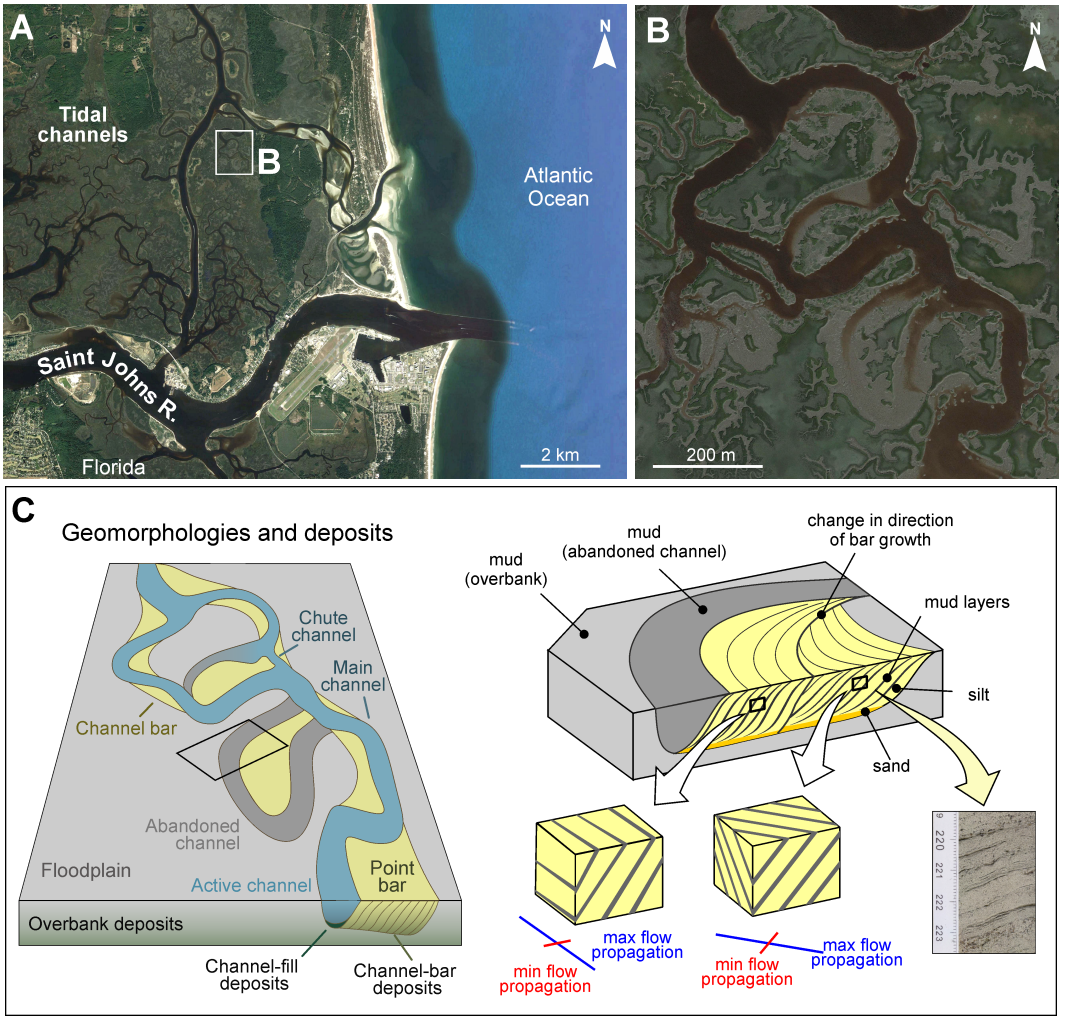

Figure 3: (A) Examples from the Florida coast of tidal and fluvial channels flowing orthogonally into the Sea. (B) Zoom in into the tidal network, (C) to recognize the main tidal elements. The abandoned channel cuts through the muddy overbank and is commonly composed of a muddy channel fill and a silty point bar. The channel can experience different transformation styles while accreting the point bar, which can be recognized in bar deposits thanks to changes in the dip direction of strata. Each package of same inclined strata shows precise 3D orientations of maximum and minimum flow, which are parallel and orthogonal to strata orientation, respectively.

4. Numerical simulations

We consider a square domain given by $\Omega = [-15, 900] \times [-205, 550]$ m×m, which contains the specific site of our experimental studies. Different simulations are run considering the variability of three main drivers: i) the regional piezometric gradient; ii) the conductivity tensor; iii) the geometry and anisotropies of the bar bodies. The main terminology related to sedimentary bodies is shown in fig. 3 C and follows sedimentological studies carried out on tidal meanders and related deposits (Cosma et al., 2019, 2020b).

The direction of the regional piezometric gradient is assumed to be parallel to the mean channel belt axis, with an average magnitude of 8×10^{-4}. This assumption aims at simulating a groundwater flow occurring in coastal plains where late Holocene buried channel belts are commonly transverse to the actual coastline. These buried formations have been generated in a paleo-landscape configuration that is fully comparable to the present-day one, and can be the main pathways for pollutant propagation to the sea, as well as suffer

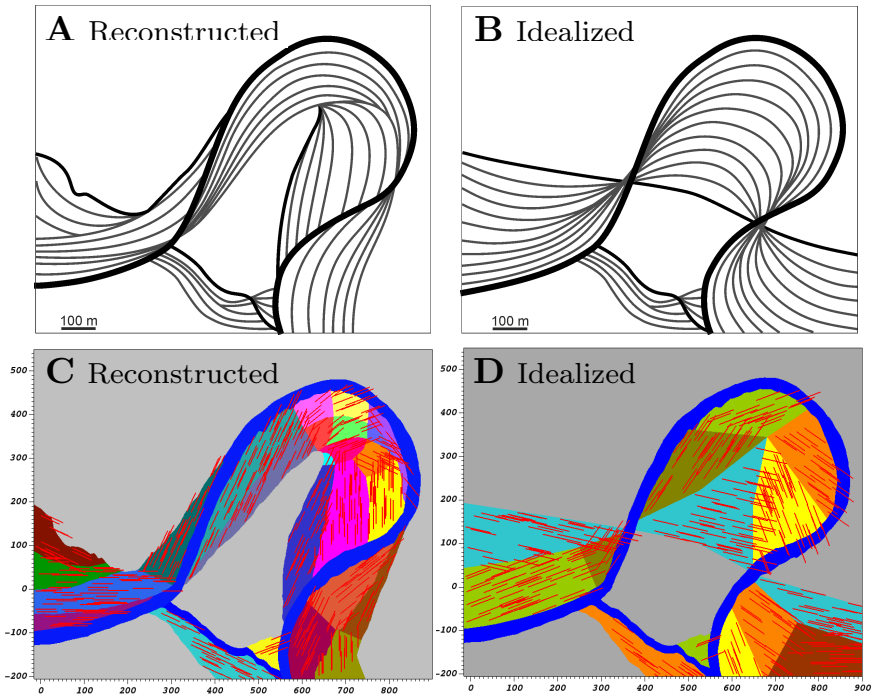

Figure 4: Model domain with reconstructed bar bodies (A, C) and idealized geometry (B, D). The corresponding preferential direction of the flow is shown by the red segments. Areas where no segments are displayed are assumed to be isotropic.

saltwater intrusion from the sea (fig. 3 A, B). Accordingly, a landward (i.e., south-east towards north-west) and seaward (i.e., north-west towards south-east) regional piezometric gradients are simulated to account for meanders migrating in different directions. In practice, linearly varying Dirichlet boundary conditions are set to simulate the two different scenarios.

Different hydraulic conductivity values are attributed to different deposits. Being uniformly made of clay-rich mud, overbank deposits show a small conductivity, estimated at $\kappa = 10^{-9}$ m/s. The actual value is not important since essentially no flow occurs in these formations. Observed channel-fill mud is assumed to have a conductivity of $\kappa = 10^{-8}$ m/s. Some simulations are also carried out with a conductivity of $\kappa = 10^{-7}$ m/s in order to model cases where a progressive channel abandonment has caused infill of the channel with coarser deposits (Allen, 1965; Fisk, 1947; Toonen et al., 2012). Bar deposits are more permeable, being made of silt and very fine sand. Since bar deposits are considered as homogeneous bodies, we associate the same conductivity values for all the bar bodies, estimated at $\kappa = 10^{-6}$ m/s. The presence of muddy laminae affects the flow mobility within the bar deposits, with maximum and minimum values occurring along the strike and dip directions, respectively. We simulate this behavior by assuming a spatially varying effective conductivity tensor $\mathbb{K}_s$ with principal directions of anisotropy that follow the strike and dip directions. We consider a constant anisotropy ratio equal to $r_a = 10^{-2}$ in the bars, while an isotropic behavior (i.e., $r_a = 1$) is imposed in the channels and external fills. Sensitivity to this ratio has been verified by using $r_a = 5 \times 10^{-3}$ with negligible differences in the relative simulations.

Contrasting bar geometries are also considered. In one set of simulations, we reconstruct the bar bodies by dividing the formations into different subregions that take into consideration the bar evolution from a sinuous channel as revealed by seismic data. The resulting subdivision is shown in fig. 4 (A, C). Correspondingly, principal directions of anisotropy follow in each subregion the reconstructed strike and dip orientations

(red lines in fig. 4). The laminae-following distribution has been implemented in the simulation model by a subdivision of the bar deposits into further subzones where constant anisotropy directions are specified.

In the second set of simulations, fluid flow is modeled using an idealized bar geometry (shown in fig. 4, B, D), established considering a uniform bar accretion from a straight channel, as commonly suggested by classical facies models (Brice, 1974; Finotello et al., 2018; Nanson and Page, 1983). Within the channel-bar bodies, both in the reconstructed and in the idealized case, anisotropies represent areas characterized by almost the same depositional orientation of the strata composing the porous media, so they are architectural. In the case of the prototype area, anisotropies are related to the different accretion packages that the channel originated during its morphodynamic evolution. Anisotropies strongly define the preferential direction of groundwater flows (fig. 4).

For the accompanying transport simulations, we have a field estimate of $n = 0.2$ [-], and we have chosen typical values for dispersion coefficients found in the literature by setting $\alpha_L = 1$ [m], $\alpha_T = 0.1$ [m] and a molecular diffusion equal to $D_m = 10^{-10}$ [m^2/s] (LaBolle and Fogg, 2001). These values yield a mesh Peclet number slightly larger than two, thus requiring stabilization. We use SUPG with optimal parameters (Bachini et al., 2021). The boundary conditions impose unit normalized concentration in the West and South portions of the boundary where the bars and the channels intersect, and zero concentration in the remaining portions, independently on the direction of the regional gradient. Note that, for a NW to SE regional gradient inflow and outflow occur at the west and south boundaries, respectively, while in the other case they occur in the south and west boundaries. No inflow would ever occur at the north and east boundaries because of extremely low conductivity values. We recall that the transport simulations are intended to highlight the effects of the different distributions of conductivity tensors within the reconstructed bars. The employed boundary conditions force the entrance of contaminants from the principal bar deposits. Different boundary conditions could have been employed depending on the geological reconstruction, but sensitivity to these effects is not of interest for this study.

4.1. Results

Figures 5 to 9 show the results of our simulations and are organized as follows. The top panels report the steady-state piezometric head distribution and the velocity vectors as calculated from the flow model. In these figures, the scale of the piezometric head measured in meters is the same for all figures. On the other hand, the scale for Darcy flux changes for each test case to ease the visualization of the vectors. The remaining four panels show the normalized concentration distributions at four different times as driven by the velocity field, using a color scale from red ($c = 1$) to blue ($c = 0$). We would like to note that the times at which we show the results are unrealistically long, but the local effects due to anisotropy that we want to show depend on the distance of the contaminant source. In our tests, the location of the contaminant source is arbitrarily chosen to highlight the importance of horizontal anisotropy. Hence, we regard our time as

The first figure in the series (fig. 5) shows our results in the case of reconstructed geometry with $\kappa_1 = 10^{-8}$ m/s and $\kappa_2 = r_a\kappa_1 = 10^{-10}$ m/s. Looking at the top panel, we see that most of the flow occurs in the southern bar of the minor channel fill (B1) and the western bar of the main channel fill (PB1). The recirculation patterns visible in the vicinity of the southern-west boundary are caused by the specific boundary conditions and the fact that bar PB1 is essentially closed by the main channel fill. A secondary flow path follows the geometry of the bars surrounding the main channel fill, the latter acting as a partial barrier between PB1 and PB2, and PB2 and PB3. The Darcy velocity vectors are approximately aligned with the directions of anisotropy, except in the channel fill crossing PB1 and PB2, where an isotropic conductivity tensor is employed. The velocities in the region external to the bars and channel fills are clearly negligible. Not so in the channel fills, although they are at least one order of magnitude smaller than in the bars, in accordance with the value of the hydraulic conductivity. We would like to remark that the linear finite element approach may yield velocity vectors that point to the wrong nonphysical direction in the presence of strong and abrupt

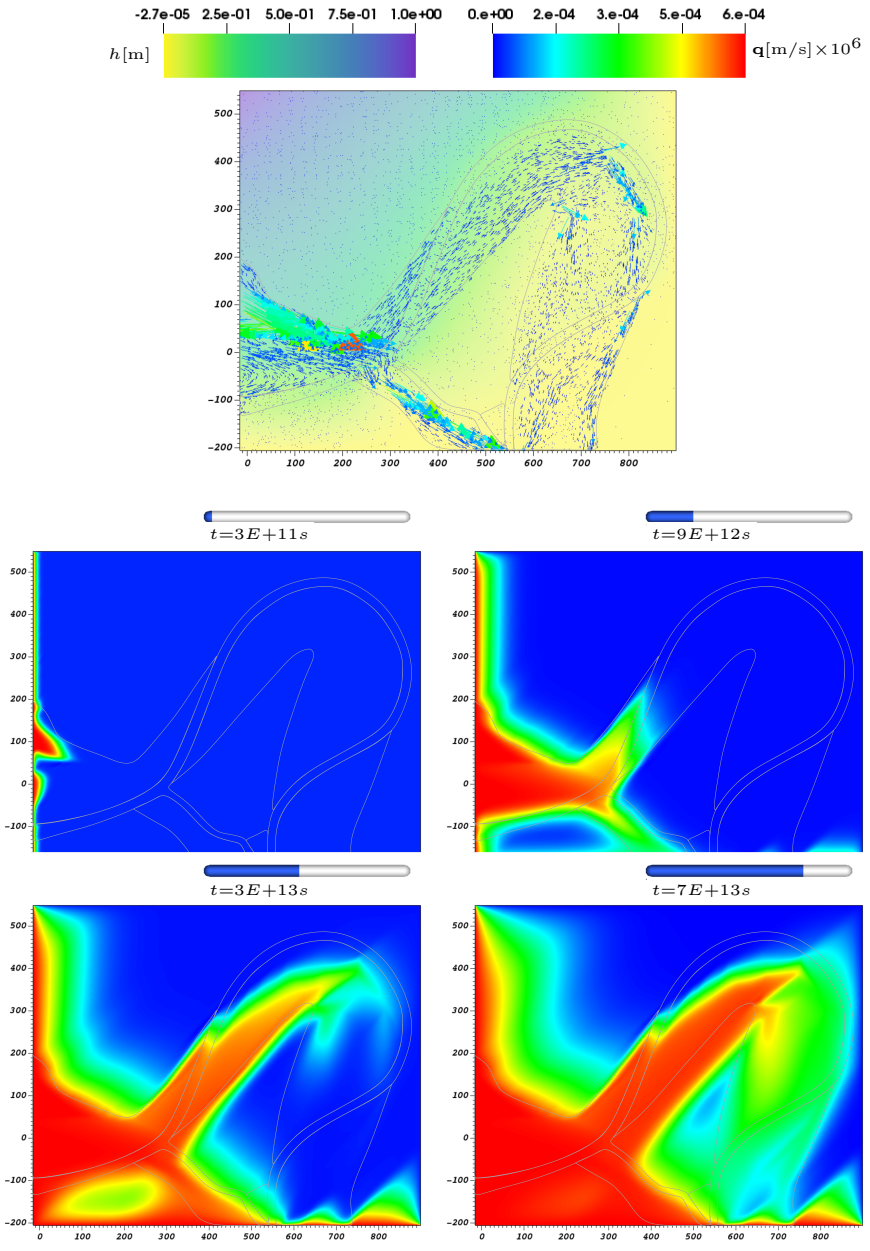

Figure 5: Reconstructed bodies and anisotropies: anisotropy ratio $r_a = 10^{-2}$, channel fill $\kappa_1 = 10^{-8}$ m/s, $\kappa_2 = r_a\kappa_1$, NW to SE gradient. Top panel: steady-state piezometric head distribution and Darcy velocities. Central and bottom panels: normalized concentration (red: $c = 1$, blue: $c = 0$) at four different times (s). The last time corresponds roughly to steady-state.

heterogeneities. This well known result, highlighted by Putti and Cordes (1998), can be overcome by the employment of appropriate mass-conservative reconstructions (Scudeler et al., 2016b). These effects can be seen in some parts of the domain but are highly localized and typically have no influence on both flow and transport processes. This phenomenon cannot be confused with the recirculation patterns that form where jumps in conductivity values or anisotropy directions are imposed. This can be seen in the lower-left part in PB1 and in the upper-right portion in PB2.

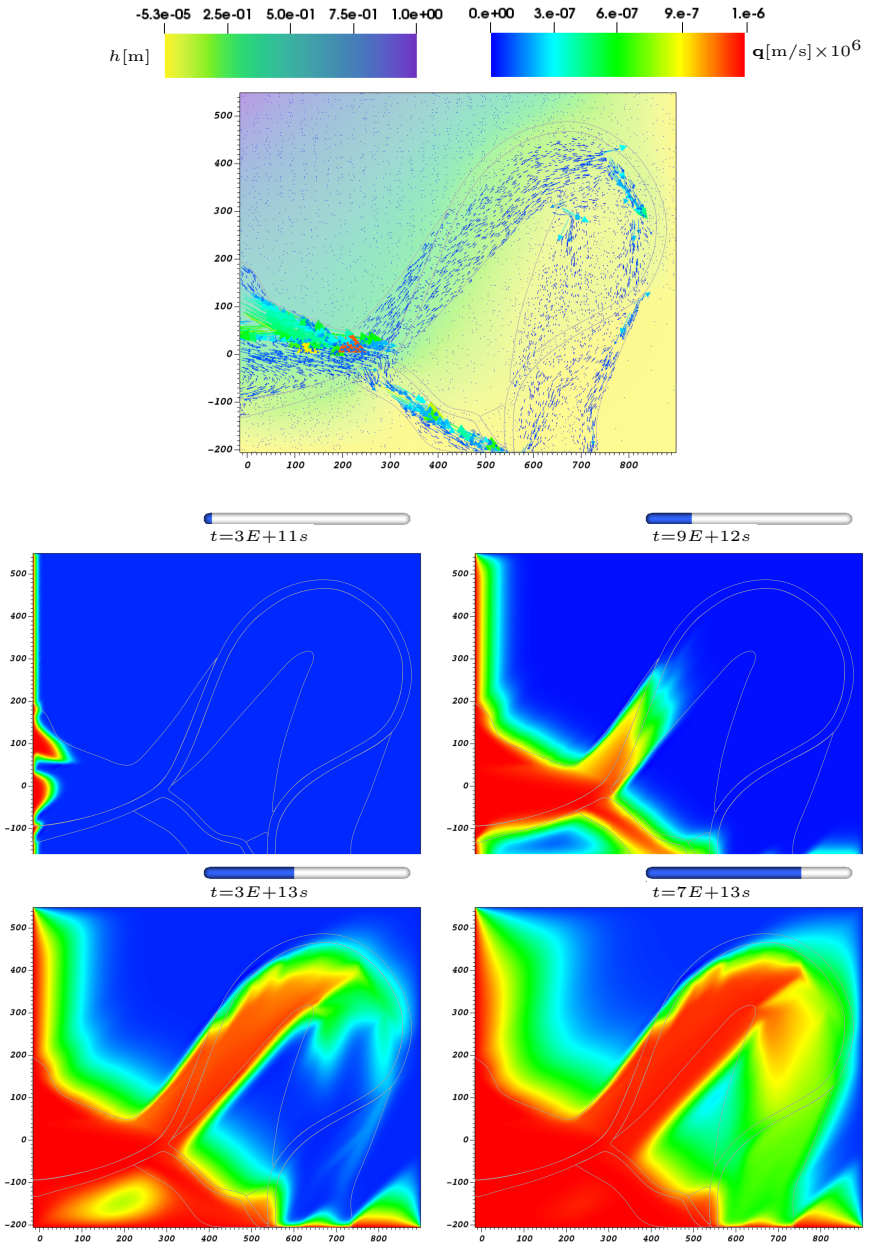

Figure 6: Reconstructed bodies and anisotropies: anisotropy ratio $r_a = 10^{-2}$, channel fill $\kappa_1 = 10^{-7}$ m/s, $\kappa_2 = r_a\kappa_1$, NW to SE gradient. Top panel: steady-state piezometric head distribution and Darcy velocities. Central and bottom panels: normalized concentration (red: $c = 1$, blue: $c = 0$) at four different times (s). The last time corresponds roughly to steady-state.

The time sequence in the transport simulation shows a plume entering from the western boundary and progressing towards the meandering bars. Once it reaches the channel fill between PB1 and PB2 the plume drastically decreases its speed (see panel at $t = 9E + 6$ s) while crossing it, as evidenced by the time differences in the solute front position in the main bars before and after the complete crossing of the channel fill. After this, the plume gains speed and progresses following the flow velocities, as dictated by the reconstructed geometry. It is interesting to note that molecular diffusion intervenes mainly at later times in

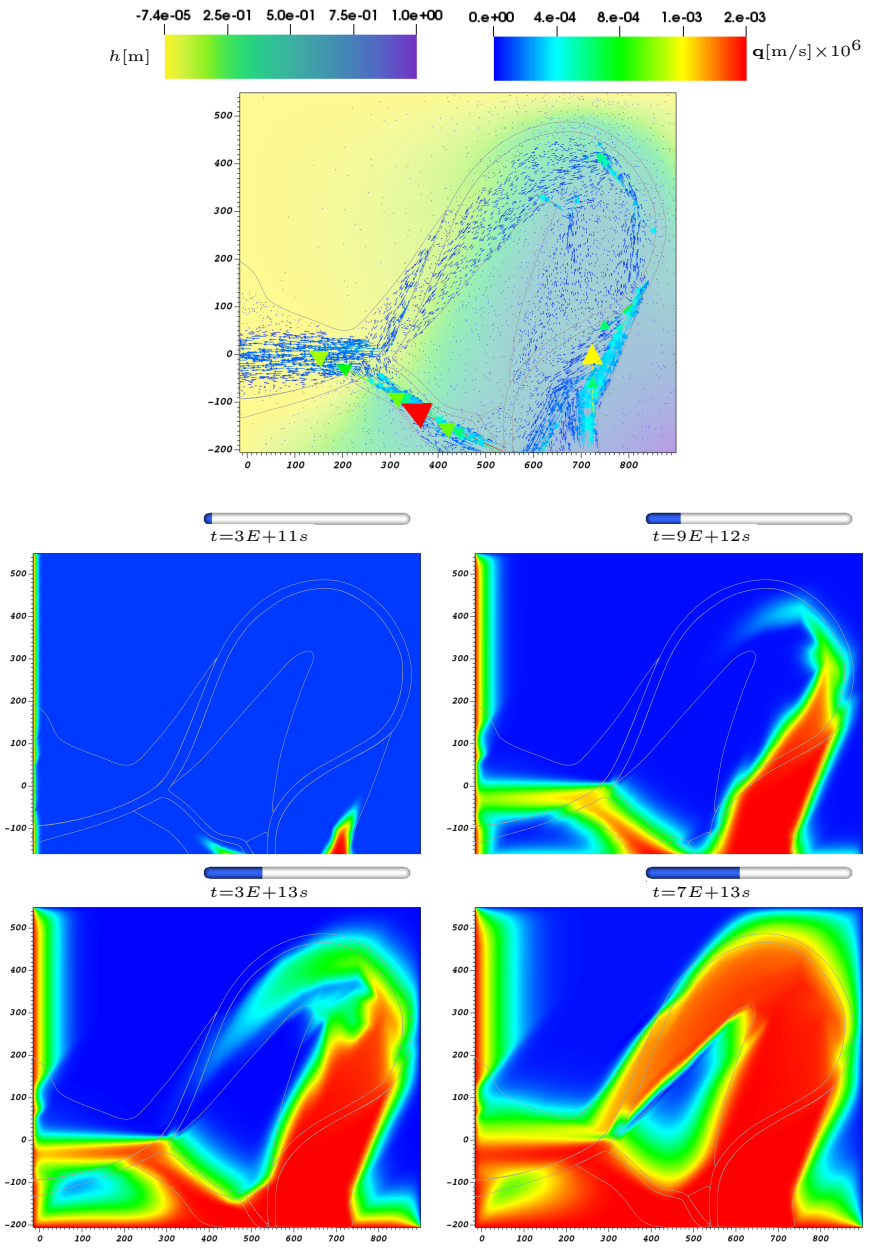

Figure 7: Reconstructed bodies and anisotropies: anisotropy ratio $r_a = 10^{-2}$, channel fill $\kappa_1 = 10^{-8}$ m/s, $\kappa_2 = r_a\kappa_1$, SE to NW gradient. Top panel: steady-state piezometric head distribution and Darcy velocities. Central and bottom panels: normalized concentration (red: $c = 1$, blue: $c = 0$) at four different times (s). The last time corresponds roughly to steady-state.

the regions where the velocities are small. Superimposed to molecular diffusion we can clearly discern the effect of variable anisotropy directions, in particular in the upper portion of the meander bar PB2.

Figure 6 shows the same results in the case of $\kappa_1 = 10^{-7}$ m/s in the channel fill. The dynamics of the process is essentially the same with a globally faster speed of propagation due to a faster crossing of the channel fill. Here the effect of the changing anisotropy directions is much more pronounced as indicated by the more distinct preferential paths in the solute movement, which causes a quicker filling of the bars.

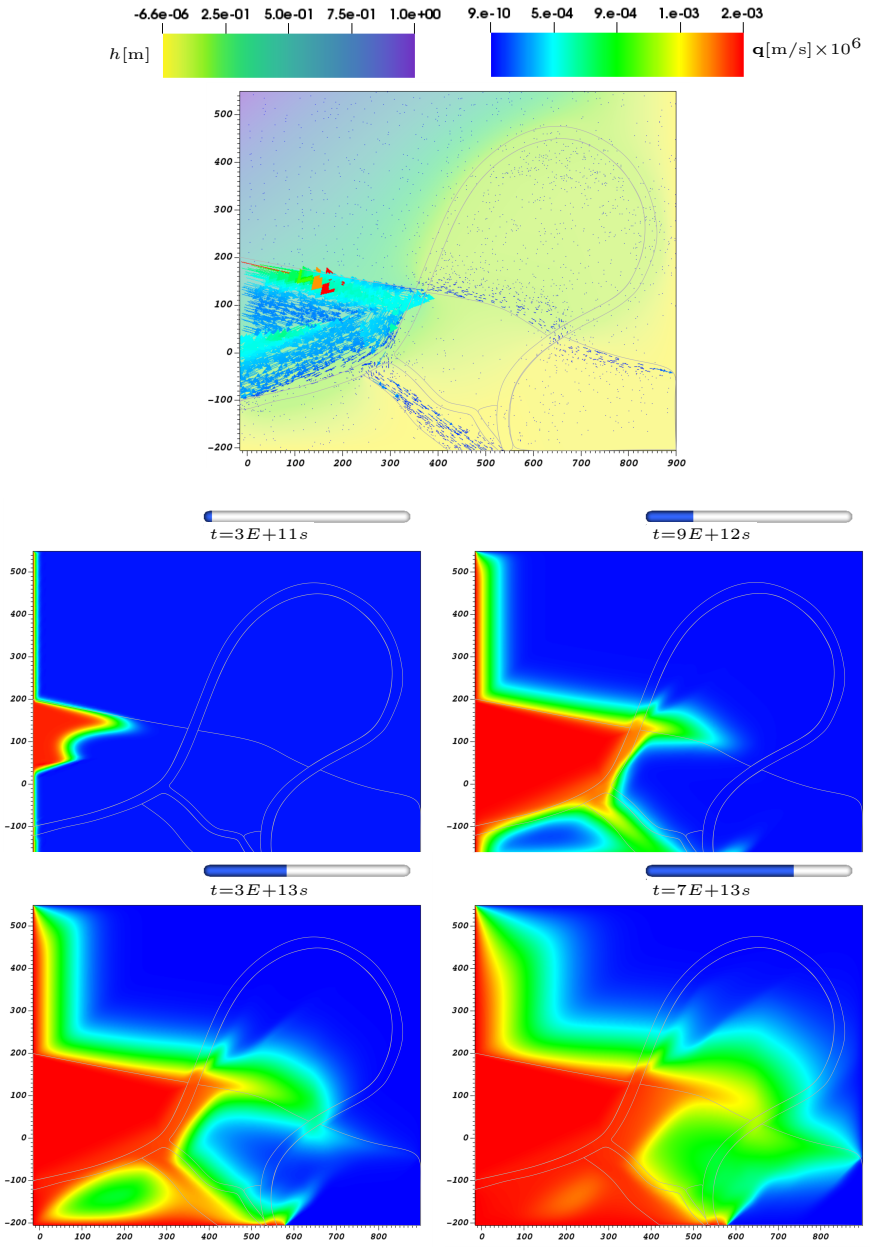

Figure 8: Idealized geometry and anisotropies: anisotropy ratio $r_a = 10^{-2}$, channel fill $\kappa_1 = 10^{-8}$ m/s, $\kappa_2 = r_a\kappa_1$, NW to SE gradient. Top panel: steady-state piezometric head distribution and Darcy velocities. Central and bottom panels: normalized concentration (red: $c = 1$, blue: $c = 0$) at four different times (s). The last time corresponds roughly to steady-state.

When the direction of the gradient is exchanged from NW-SE to SE-NW (fig. 7) contaminant intrusion is more prominent because the channel fill is farther from the inflow boundary than in the previous simulations. All the flow and transport details remain essentially the same as described before.

The scenario changes completely when we use the idealized bar geometry (see fig. 4 B, D). Indeed, fig. 8 and 9, which represent the results of the simulation in the case of the NW-SE and SE-NW imposed regional gradients, respectively, clearly show that the contaminant does not enter the meander bar PB2 and PB3. Since

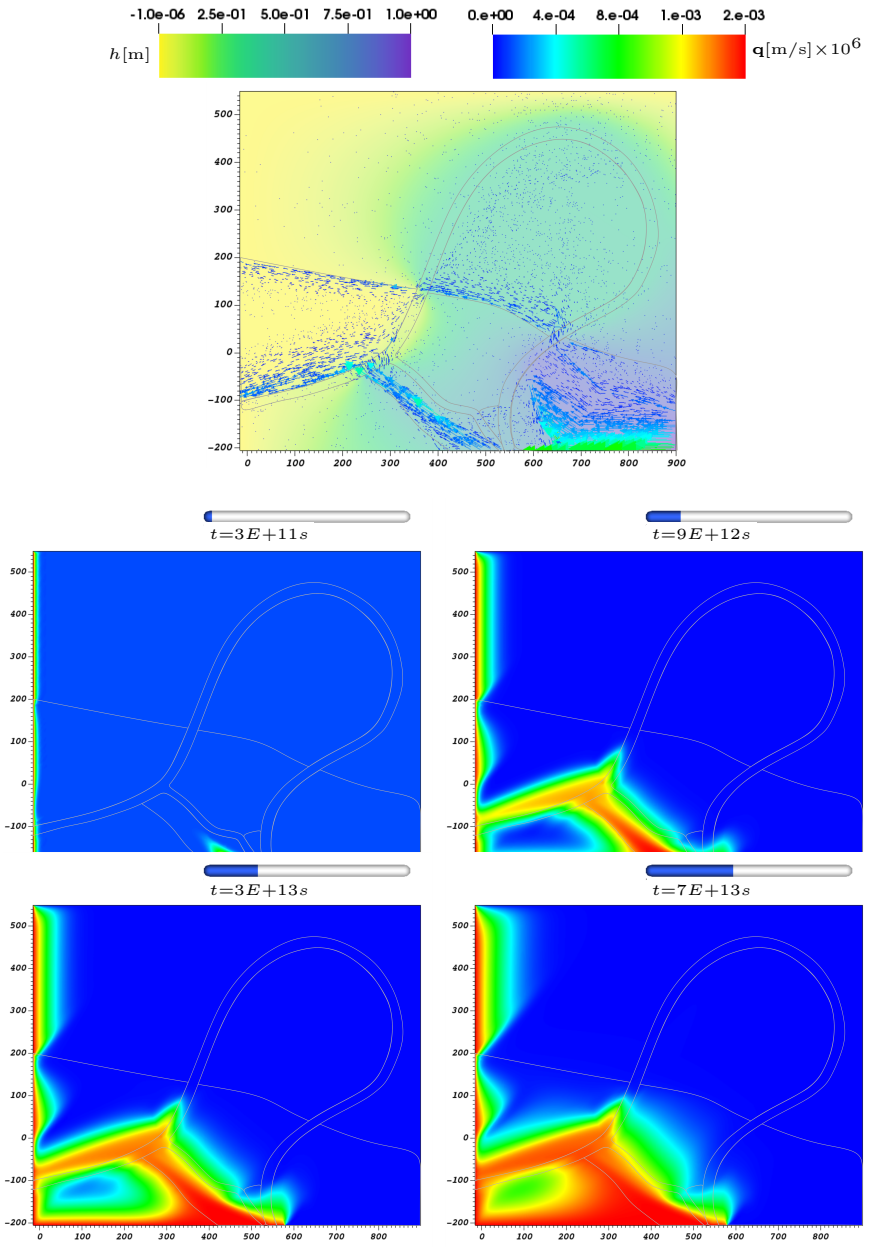

Figure 9: Idealized geometry and anisotropies: anisotropy ratio $r_a = 10^{-2}$, channel fill $\kappa_1 = 10^{-8}$ m/s, $\kappa_2 = r_a\kappa_1$, SE to NW gradient. Top panel: steady-state piezometric head distribution and Darcy velocities. Central and bottom panels: normalized concentration (red: $c = 1$, blue: $c = 0$) at four different times (s). The last time corresponds roughly to steady-state.

the magnitude of the hydraulic conductivity is the same in both reconstructed and idealized geometries, the difference must be ascribed entirely to the effects of anisotropy. This shows the importance of an accurate reconstruction not only of the geological formations but also their hydraulic characteristics.

4.2. Discussion

Several studies report the importance of having interconnected permeable channelized bodies to guarantee fluid flow in the subsurface (Donselaar and Overeem, 2008; Willems et al., 2017; Willis and

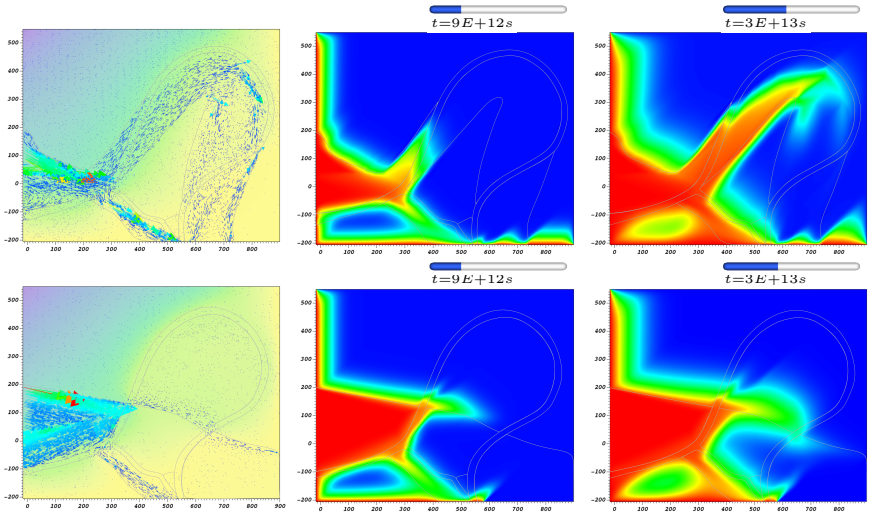

Figure 10: Comparison of flow velocities and concentration distributions in the cases of reconstructed (top panels) and idealized (bottom panels) geometries and anisotropies: anisotropy ratio $r_a = 10^{-2}$, channel fill $\kappa_1 = 10^{-8}$ m/s, $\kappa_2 = r_a\kappa_1$, NW to SE gradient.

Tang, 2010; Yan et al., 2019). The sedimentary record of meandering tidal channels comprises sand-prone in channel elements (e.g., channel-bar deposits) and muddy over-bank deposits. Channel bars, which accumulated during the lateral migration of a channel, are the most permeable bodies developed by tidal networks and the emerging flow patterns are directly related to their intra- and inter-connectivity (Pranter et al., 2007; Willis and Sech, 2018a). Channel-fill deposits, which accumulated within the channel during its deactivation, are less permeable since they commonly exhibit a basal sandy layer covered by a plug fill (Allen, 1965; Brivio et al., 2016; Donselaar and Overeem, 2008; Jackson et al., 2005; Toonen et al., 2012; D'Alpaos et al., 2017). Over-bank deposits (e.g., tidal flats) are considered almost impermeable as they are composed of mostly fine sediments by (mud and peat layers). Subsurface deposits of reclaimed coastal areas were commonly generated in tidal networks, and fluid flow within these sediments is governed by their sedimentary features and stratal patterns, which originated during the morphodynamic evolution of tidal channels (Brivio et al., 2016; Choi and J.H., 2015; Dashtgard et al., 2012; Dashtgard and La Croix, 2015; Ghinassi et al., 2018b; La Croix and Dashtgard, 2015).

Variability of growth styles shown by the prototype bars is at the origin of the emerging complex internal architecture (Willis and Sech, 2018a,b; Yan et al., 2019). The associated accumulation of mud layers with a variable spatial orientation has a strong impact on flow motion within the bar. Numerical results clearly show that flow develops within the bar in directions parallel to the strike of muddy layers, where conductivity is higher. Over a local scale (i.e., the bar scale), this configuration causes flow paths that can strongly disagree with the regional groundwater gradient (Willis and Tang, 2010). Additionally, the lateral pinching out of accretionary packages causes internal compartmentalization of the bar with further local reduction of flux magnitudes. The simulation of this variability has been effectively achieved by modeling the flow behavior using a planar anisotropic conductivity tensor adapted to the sedimentation history. Following this framework, our numerical test with opposing piezometric gradients does not provide significantly different flow patterns but highlights the important role of intra-bar anisotropies in seaward or landward fluids.

The choice to compare simulation results based on reconstructed and idealized bar complexes highlights the importance of accurate 3D geometric modeling of the subsurface deposits to properly predict groundwater flows. The use of simplistic models (Brice, 1974; Finotello et al., 2018; Lewin, 1976; Nanson and Page,

1983; Wu et al., 2015) can underestimate the effective permeable volume in the subsoil, as shown by Bellizia et al. (2021); Cassiani et al. (2020), thus limiting the accuracy of the prediction of the effective propagation styles (see fig. 10). Specifically, in the numerical simulations of the idealized case, subsurface flow in the point bar opposite to the inflow boundary (i.e., within PB2 and PB3, in simulations with the NW-SE oriented gradient, and PB2 and PB1 in simulations with the SE-NW oriented gradient) is negligible, as shown in fig. 8 and fig. 9. Indeed, in the idealized belt contaminant propagation is hindered where adjacent bars connect only at the channel inflection point. On the other hand, in the reconstructed case, the flow is constrained by the channel fill but hydraulic gradients propagate across giving rise to non-negligible Darcy velocities in the neighboring bars. For this reason, contaminants propagate in the bar following the directions of anisotropy if given enough time to cross the channel fill.

Since the accretion mechanisms of the different structures are responsible for the architectural anisotropies of the permeable bodies, the study case highlights how performing a thorough stratal evolution reconstruction of a channelized system is crucial to correctly predict groundwater flows. Especially within PB2, anisotropies play a key role in the fluid motion. Darcy velocities show marked changes in their orientation close to the apex zone according to the principal directions of anisotropy, thus remaining confined within the bar body. On the other hand, anisotropies in the idealized belt have gentler boundaries, allowing the formation of smoother trajectories (fig. 4). However, our results show that the cross-bar channels control fluid motion. Indeed, chute channels are associated with cut-off mechanisms as they cut through a meander bend shortening the channel length (Constantine et al., 2010; Ghinassi, 2011; McGowen and Garner, 1970). In our simulations, the entire minor channel system acts as a preferential pathway connecting PB1 and PB3 in both landward and seaward regional flow, effectively disconnecting in the idealized case PB2 from the active flow region. In the simulations with the two gradient orientations, the highest Darcy velocities are observed in the B1 body, which is the more extended bar of the minor channel system, whereas B2 is practically isolated from the overall permeable system due to its position with respect to the main and minor channel fills. Overall, these simulations highlight that minor channel systems strongly act as preferential pathways when they are almost parallel to the main channel belt axis.

Simulations in the study case reveal that the grain-size composition of the channel fill strongly affects the connectivity between adjacent bar bodies by its influence on the hydraulic properties of the formation, as highlighted by several studies (Ambrose et al., 1991; Donselaar and Overeem, 2008; Pranter et al., 2007; Willis and Tang, 2010). Channel fills with sedimentary facies similar to those of the related bar deposits allow a better interconnection between adjacent bars than channel fills characterized by lower conductivity values. Simulations with the two different $\mathbb{K}_s$ for the channel fills remark this feature. Note that, contrary to our prototype case of tidal origin, fluvial paleo channels may exhibit higher differences between the conductivity of the channel fill and the bar bodies.

Acknowledgments

This work was sponsored by “HYDROSEM: Fluvial and tidal meanders of the Venetian-Po plain: from hydrodynamics to stratigraphy” project (Progetto di Eccellenza CARIPARO 2017, PI Massimiliano Ghinassi) and University of Padova (SID2016 project, titled “From channels to rock record: morphodynamic evolution of tidal meanders and related sedimentary products”, PI Massimiliano Ghinassi). Authors are thankful to S. Donnici (IGG, CNR Padova) and F. Madricardo (ISMAR, CNR Venezia) for providing geophysical and core data obtained in the frame of “ECHOS” project (Ministero delle Infrastrutture e dei Trasporti- Provveditorato Interregionale per le Opere Pubbliche del Veneto - Trentino Alto Adige - Friuli Venezia Giulia, Consorzio Venezia Nuova).

References

Allen, J., 1965. A review of the origin and characteristics of recent alluvial sediments. Sedimentology 5, 89–191. doi:10.1111/j.1365-3091.1965.tb01561.x.

Ambrose, W., Tyler, N., Parsley, M., 1991. Facies heterogeneity, pay continuity, and infill potential in barrier-island, fluvial, and submarine-fan reservoirs: Examples from the texas gulf coast and midland basin, in: Miall, A., Tyler, N. (Eds.), The Three-Dimensional Facies Architecture of Terrigenous Clastic Sediments, and Its Implications for Hydrocarbon Discovery and Recovery: SEPM Concepts in Sedimentology and Paleontology. Cambridge University Press. volume 3, pp. 13–21. doi:10.2110/csp.91.03.

Amorosi, A., Bini, M., Giacomelli, S.and Pappalardo, M., Ribecai, C., Rossi, V., Sammartino, I., Sarti, G., 2013. Middle to late holocene environmental evolution of the pisa coastal plain (Tuscany, Italy) and early human settlements. Quat. Int 303, 93–106. doi:10.1016/j.quaint.2013.03.030.

Bachini, E., Farthing, M.W., Putti, M., 2021. Intrinsic finite element method for advection-diffusion-reaction equations on surfaces. J. Comp. Phys. 424. doi:10.1016/j.jcp.2020.109827.

Bear, J., 1979. Hydraulics of groundwater. McGraw-Hill.

Bellizia, E., Boaga, J., Fontana, A., D'Alpaos, A., Cassiani, G., Ghinassi, M., 2021. Impact of genesis and abandonment processes of a fluvial meander on geometry and grain-size distribution of the associated point bar (Venetian Plain, Italy). Mar. Pet. Geol. 127, 104951. doi:10.1016/j.marpetgeo.2021.104951.

Bellizia, E., Donnici, S., Madricardo, F., Finotello, A., D'Alpaos, A., Ghinassi, M., 2022. Ontogeny of a subtidal point bar in the microtidal Venice Lagoon (Italy) revealed by three-dimensional architectural analyses. Sedimentology n/a. doi:https://doi.org/10.1111/sed.12956.

Benner, S., Polizzotto, M., Kocar, B., Ganguly, S., Phan, K., Ouch, K., Sampson, M., Fendorf, S., 2008. Groundwater flow in an arsenic-contaminated aquifer, Mekong Delta, Cambodia. Appl. Geochemistry 23, 3072–3087. doi:10.1016/j.apgeochem.2008.06.013.

Boyer, P., Roberts, N., Baird, D., 2006. Holocene environment and settlement on the Çarşamba alluvial fan, south-central Turkey: Integrating geoarchaeology and archaeological field survey. Geoarchaeology 21, 675–698. doi:10.1002/gea.20133.

Brice, J., 1974. Evolution of meander loops. Geol. Soc. Am. Bull. 85, 581—586. doi:10.1130/0016-7606(1974)85<581:EOML>2.0.CO;2.

Bridge, J., 2003. Rivers and floodplains. Forms, Processes and Sedimentary Record. Blackwell Science, Ltd.

Brivio, L., Ghinassi, M., D'Alpaos, A., Finotello, A., Fontana, A., Roner, M., Howes, N., 2016. Aggradation and lateral migration shaping geometry of a tidal point bar: An example from salt marshes of the Northern Venice Lagoon (Italy). Sediment. Geol. 343, 141—-155. doi:10.1016/j.sedgeo.2016.08.005.

Camporese, M., Paniconi, C., Putti, M., Orlandini, S., 2010. Surface-subsurface flow modeling with path-based runoff routing, boundary condition-based coupling, and assimilation of multisource observation data. Water Resour. Res. 46, W02512. doi:10.1029/2008WR007536.

Carraro, A., Fabbri, P., Giaretta, A., Peruzzo, L., Tateo, F., Tellini, F., 2013. Arsenic anomalies in shallow Venetian plain (northeast Italy) groundwater. Environ. Earth Sci. 70, 3067—-3084. doi:10.1007/s12665-013-2367-2.

Carraro, A., Fabbri, P., Giaretta, A., Peruzzo, L., Tateo, F., Tellini, F., 2015. Effects of redox conditions on the control of arsenic mobility in shallow alluvial aquifers on the Venetian plain (Italy). Sci. Total Environ. 532, 581—594. doi:10.1016/j.scitotenv.2015.06.003.

Cassiani, G., Bellizia, E., Fontana, A., Boaga, J., D'Alpaos, A., Ghinassi, M., 2020. Geophysical and sedimentological investigations integrate remote-sensing data to depict geometry of fluvial sedimentary bodies: An example from Holocene point-bar deposits of the Venetian Plain (Italy). Remote Sens. 12, 2568. doi:10.3390/rs1216256.

Choi, K., J.H., J., 2015. Morphodynamics of tidal channels in the open coast macrotidal flat, Southern Ganghwa Island in Gyeonggi Bay, west coast of Korea. J. Sediment. Res. 85, 582–595. doi:10.2110/jsr.2015.44.

Christensen, B., Hatfield, K., 1994. In situ restoration of contaminated surficial aquifers. part i: The flow process. in: IAHS Publications - Series of Proceedings and Reports-Intern . Assoc. Hydrological Sciences , 313—322.

Constantine, J., McLean, S., Dunne, T., 2010. A mechanism of chute cutoff along large meandering rivers with uniform floodplain topography. Geol. Soc. Am. Bull. 122, 855–869. doi:10.1130/B26560.1.

Cosma, M., Finotello, A., Ielpi, A., Ventra, D., Oms, O., D'Alpaos, A., Ghinassi, M., 2020a. Piracy-controlled geometry of tide-dominated point bars: Combined evidence from ancient sedimentary successions and modern channel networks. Geomorphology 370, 107402. doi:https://doi.org/10.1016/j.geomorph.2020.107402.

Cosma, M., Ghinassi, M., D'Alpaos, A., Roner, M., Finotello, A., Tommasini, L., Gatto, R., 2019. Point-bar brink and channel thalweg trajectories depicting interaction between vertical and lateral shifts of microtidal channels in the Venice Lagoon (Italy). Geomorphology 342, 37–50. doi:10.1016/j.geomorph.2019.06.009.

Cosma, M., Yan, N., Colombera, L., Mountney, N.P., D'Alpaos, A., Ghinassi, M., 2020b. An integrated approach to determine three-dimensional accretion geometries of tidal point bars: Examples from the Venice Lagoon (Italy). Sedimentology doi:10.1111/sed.12787.

Da Lio, C., Carol, E., Kruse, E., Teatini, P., Tosi, L., 2015. Saltwater contamination in the managed low-lying farmland of the Venice coast, Italy: An assessment of vulnerability. Sci. Total Environ. 533, 356—369. doi:10.1016/j.scitotenv.2015.07.013.

D'Alpaos, A., Ghinassi, M., Finotello, A., Brivio, L., Bellucci, L.G., Marani, M., 2017. Tidal meander migration and dynamics: A case study from the Venice Lagoon. Mar. Pet. Geol. 87, 80–90. doi:10.1016/j.marpetgeo.2017.04.012.

Dashtgard, S., La Croix, A., 2015. Sedimentological trends across the tidal–fluvial transition, Fraser River, Canada: A review and some broader implications, in: Ashworth, P., Best, J., Parsons, D. (Eds.), Fluvial -Tidal Sedimentology. Elsevier. Developments in Sedimentology, pp. 111–126. doi:10.1016/B978-0-444-63529-7.00005-5.

Dashtgard, S., Venditti, J., Hill, P., Johnson, S., La Croix, A., 2012. Sedimentation across the tidal-fluvial transition in the Lower Fraser River , Canada. Sediment. Rec. 10, 4–9. doi:10.2110/sedred.2012.4.4.

Delagnes, A., Tribolo, C., Bertran, P., Brenet, M., Crassard, R., Jaubert, J., Khalidi, L., Mercier, N., Nomade, S., Peigné, S., Sitzia, L., Tournepiche, J., Al-Halibi, M., Al-Mosabi, A.and MacChiarelli, R., 2012. Inland human settlement in southern Arabia 55,000 years ago. New evidence from the Wadi surdud middle paleolithic site complex, western Yemen. J. Hum. Evol. 63, 452–474. doi:10.1016/j.jhevol.2012.03.008.

Desbarats, A., Koenig, C., Pal, T., Mukherjee, P., Beckie, R., 2014. Groundwater flow dynamics and arsenic source characterization in an aquifer system of west bengal, india. Water Resour. Res. 50, 4974–5002. doi:10.1002/2013WR014034.

Donselaar, M., Overeem, I., 2008. Connectivity of fluvial point-bar deposit: An example from the Miocene Huesca fluvial fan, Ebro Basin, Spain. Am. Assoc. Pet. Geol. Bull. 92, 1109–1129. doi:10.1306/04180807079.

D'Alpaos, A., Carniello, L., Rinaldo, A., 2013. Statistical mechanics of wind wave-induced erosion in shallow tidal basins: Inferences from the Venice lagoon. Geophys. Res. Lett. 40, 3402—3407. doi:10.1002/grl.50666.

Finotello, A., Canestrelli, A., Carniello, L., Ghinassi, M., D'Alpaos, A., 2019. Tidal flow asymmetry and discharge of lateral tributaries drive the evolution of a microtidal meander in the Venice Lagoon (Italy). J. Geophys. Res. Earth Surf. 124, 3043–3066. doi:10.1029/2019JF005193.

Finotello, A., Ghinassi, M., Carniello, L., Belluco, E., Pivato, M., Tommasini, L., D'Alpaos, A., 2020. Three-dimensional flow structures and morphodynamic evolution of microtidal meandering channels. Water Resour. Res. 56. doi:10.1029/2020WR027822.

Finotello, A., Lanzoni, S., Ghinassi, M., Marani, M., Rinaldo, A., D'Alpaos, A., 2018. Field migration rates of tidal meanders recapitulate fluvial morphodynamics. Proc. Natl. Acad. Sci. U.S.A. 115, 1468. doi:10.1073/pnas.1711330115.

Fisk, H., 1947. Fine-grained alluvial deposits and their effects on Mississippi River activity. Vols 1-2. Mississippi River Commission, Vicksburg, MS.

Fogg, G.E., Carle, S.F., Green, C., 2000. Connected-network paradigm for the alluvial aquifer system. Special paper-Geological Society of America , 25–42.

Fogg, G.E., Noyes, C.D., Carle, S.F., 1998. Geologically based model of heterogeneous hydraulic conductivity in an alluvial setting. Hydrogeology Journal 6, 131–143.

Ghinassi, M., 2011. Chute channels in the holocene high-sinuosity river deposits of the Firenze plain, Tuscany, Italy. Sedimentology 58, 618–642. doi:0.1111/j.1365-3091.2010.01176.x.

Ghinassi, M., Brivio, L., D'Alpaos, A., Finotello, A., Carniello, L., Marani, M., Cantelli, A., 2018a. Morphodynamic evolution and sedimentology of a microtidal meander bend of the Venice Lagoon (Italy). Mar. Pet. Geol. 96, 391–404. doi:10.1016/j.marpetgeo.2018.06.011.

Ghinassi, M., D'alpaos, A., Gasparotto, A., Carniello, L., Brivio, L., Finotello, A., Roner, M., Franceschinis, E., Realdon, N., Howes, N., Cantelli, A., 2018b. Morphodynamic evolution and stratal architecture of translating tidal point bars: Inferences from the northern Venice Lagoon (Italy). Sedimentology 65, 1354–1377. doi:10.1111/sed.12425.

Ghinassi, M., Fidolini, F., Magi, M., Sagri, M., 2013. Depositional environments of the Plio-Pleistocene Upper Valdarno Basin (Tuscany, Italy). Italian Journal of Geosciences 132, 33–53.

Gibling, M.R., 2006. Width and Thickness of Fluvial Channel Bodies and Valley Fills in the Geological Record: A Literature Compilation and Classification. J. Sediment. Res. 76, 731–770. doi:10.2110/jsr.2006.060.

Haitjema, H.M., Anderson, M.P., 2016. Darcy velocity is not a velocity. Groundwater 54, 1–1.

Harvey, C., Ashfaque, K., Yu, W., Badruzzaman, A., Ali, M., Oates, P., Michael, H., Neumann, R., Beckie, R., Islam, S., Ahmed, M., 2006. Groundwater dynamics and arsenic contamination in Bangladesh. Chem. Geol. 228, 112–136. doi:10.1016/j.chemgeo.2005.11.025.

Hatfield, K., Christensen, B., 1994. In situ restoration of contaminated surficial aquifers. part ii: The chemical process. in: IAHS Publications - Series of Proceedings and Reports-Intern . Assoc. Hydrological Sciences , 323–332.

Jackson, M., Yoshida, S., Muggeridge, A., Johnson, H., 2005. Three-dimensional reservoir characterization and flow simulation of heterolithic tidal sandstones. Am. Assoc. Pet. Geol. Bull. 89, 507–528. doi:10.1306/11230404036.

Khan, I., Bridge, J., Kappelman, J., Wilson, R., 1997. Evolution of miocene fluvial environments, eastern Potwar plateau, northern Pakistan. Sedimentology 44, 221–251. doi:10.1111/j.1365-3091.1997.tb01522.x.

Kollet, S., Sulis, M., Maxwell, R.M., Paniconi, C., Putti, M., Bertoldi, G., Coon, E.T., Cordano, E., Endrizzi, S., Kikinzon, E., Mouche, E., Mügler, C., Park, Y.J., Refsgaard, J.C., Stisen, S., Sudicky, E., 2017. The integrated hydrologic model intercomparison project, IH-MIP2: A second set of benchmark results to diagnose integrated hydrology and feedbacks. Water Resour. Res. 53, 867–890. doi:10.1002/2016WR019191.

La Croix, A., Dashtgard, S., 2015. A synthesis of depositional trends in intertidal and upper subtidal sediments across the tidal–fluvial transition in the Fraser River, Canada. J. Sediment. Res. 85, 683–698. doi:10.2110/jsr.2015.47.

LaBolle, E.M., Fogg, G.E., 2001. Role of Molecular Diffusion in Contaminant Migration and Recovery in an Alluvial Aquifer System. Transp. Porous. Med. 42, 155–179. doi:10.1023/A:1006772716244.

Lewin, J., 1976. Initiation of bed forms and meanders in coarse-grained sediment. Geol. Soc. Am. Bull. 87, 281–285. doi:10.1130/0016-7606(1976)87<281:IOBFAM>2.0.CO;2.

Madricardo, F., Donnici, S., Lezziero, A., De Carli, F., Buogo, S., Calicchia, P., Boccardi, E., 2007. Palaeoenvironment reconstruction in the lagoon of venice through wide-area acoustic surveys and core sampling. Estuar. Coast. Shelf Sci. 75, 205–213. doi:10.1016/j.ecss.2007.02.031.

Manzini, G., Putti, M., 2007. Mesh locking effects in the finite volume solution of 2-D anisotropic diffusion equations. J. Comp. Phys. 220, 751–771. doi:10.1016/j.jcp.2006.05.026.

de Marsily, G., 1986. Quantitative hydrogeology. Groundwater hydrology for engineers. Academic Press, New York.

Maxwell, R., Putti, M., Meyerhoff, S., d. Delfs, J., e. Ferguson, I., Ivanov, V., Kim, J., g. Kolditz, O., Kollet, S., Kumar, M., Lopez, S., Niu, J., Paniconi, C., Park, Y., Phanikumar, M., Shen, C., Sudicky, E., Sulis, M., 2014. Surface-subsurface model intercomparison: A first set of benchmark results to diagnose integrated hydrology and feedbacks. Water Resour. Res. 50. doi:10.1002/2013WR013725.

Mazzia, A., Manzini, G., Putti, M., 2011. Bad behavior of Godunov mixed methods for strongly anisotropic advection-dispersion equations. J. Comp. Phys. 230, 8410–8426. doi:10.1016/j.jcp.2011.07.021.

McGowen, J., Garner, L., 1970. Physiographic features and stratification types of coarse-grained pointbars: modern and ancient examples. Sedimentology 14, 77–111. doi:10.1111/j.1365-3091.1970.tb00184.x.

Nanson, G., Page, K., 1983. Lateral accretion of fine-grained concave benches on meandering rivers, in: Modern and Ancient Fluvial Systems. John Wiley & Sons, Ltd, pp. 133–143. doi:10.1002/9781444303773.ch10.

Nofal, E., Amer, M., El-Didy, S., Fekry, A., 2015. Delineation and modeling of seawater intrusion into the nile delta aquifer: A new perspective. Water Sci. 29, 156–166. doi:10.1016/j.wsj.2015.11.003.

Passadore, G., Monego, M., Altissimo, L., Sottani, A., Putti, M., Rinaldo, A., 2012. Alternative conceptual models and the robustness of groundwater management scenarios in the multi-aquifer system of the central veneto basin, italy. Hydrogeol. J. 20, 419–433. doi:10.1007/s10040-011-0818-y.

Pauloo, R.A., Fogg, G.E., Guo, Z., Henri, C.V., 2021. Mean flow direction modulates non-fickian transport in a heterogeneous alluvial aquifer-aquitard system. Water Resources Research 57, e2020WR028655.

Pranter, M., Ellison, A., Cole, R., Patterson, P., 2007. Analysis and modeling of intermediate-scale reservoir heterogeneity based on a fluvial point-bar outcrop analog, Williams Fork Formation, Piceance Basin, Colorado. Am. Assoc. Pet. Geol. Bull. 91, 1025–1051. doi:10.1306/02010706102.

Purkis, S.J., Vlaswinkel, B., 2012. Visualizing lateral anisotropy in modern carbonates. AAPG Bulletin 96, 1665–1685. doi:10.1306/02211211173.

Putti, M., Cordes, C., 1998. Finite element approximation of the diffusion operator on tetrahedra. SIAM J. Sci. Comput. 19, 1154–1168. doi:10.1137/S1064827595290711.

Renard, P., de Marsily, G., 1997. Calculating equivalent permeability: a review. Adv. Water Resour. 20, 253–278.

Scudeler, C., Pangle, L., Pasetto, D., Niu, G.Y., Volkmann, T., Paniconi, C., Putti, M., Troch, P., 2016a. Multiresponse modeling of variably saturated flow and isotope tracer transport for a hillslope experiment at the Landscape Evolution Observatory. Hydrol. Earth Syst. Sc. 20, 4061–4078. doi:10.5194/hess-20-4061-2016.

Scudeler, C., Putti, M., Paniconi, C., 2016b. Mass-conservative reconstruction of galerkin velocity fields for transport simulations. Adv. Water Resour. 94, 470–485. doi:10.1016/j.advwatres.2016.06.011.

Şimşek, C., Gemici, U., Filiz, S., 2008. An assessment of surficial aquifer vulnerability and groundwater pollution from a hazardous landfill site, Torbali/Turkey. Geosci. J. 12, 69–82. doi:10.1007/s12303-008-0009-6.

Toonen, W., Kleinhans, M., Cohen, K., 2012. Sedimentary architecture of abandoned channel fills. Earth Surf. Process. Landf. 37, 459–472. doi:10.1002/esp.3189.

Weill, S., Mazzia, A., Paniconi, C., Putti, M., 2011. Coupling water flow and solute transport into a physically-based surface–subsurface hydrological model. Adv. Water Resour. 34, 128–136. doi:10.1016/j.advwatres.2010.10.001.

Weissmann, G.S., Zhang, Y., Fogg, G.E., Mount, J.F., 2004. Influence of Incised-Valley-Fill Deposits on Hydrogeology of a Stream-Dominated Alluvial Fan, in: Aquifer Characterization. SEPM Society for Sedimentary Geology.

Willems, C., Nick, H., Donselaar, M., Weltje, G., Bruhn, D., 2017. On the connectivity anisotropy in fluvial hot sedimentary aquifers and its influence on geothermal doublet performance. Geothermics 65, 222–233. doi:10.1016/j.geothermics.2016.10.002.

Willis, B., Sech, R., 2018a. Emergent facies patterns within fluvial channel belts, in: Fluvial Meanders and Their Sedimentary Products in the Rock Record. John Wiley & Sons. number Publ. 48 in Int. Assoc. Sedimentol. Spec., pp. 509–542. doi:10.1002/9781119424437.ch19.

Willis, B., Sech, R., 2018b. Quantifying impacts of fluvial intra-channel-belt heterogeneity on reservoir behaviour, in: Fluvial Meanders and Their Sedimentary Products in the Rock Record. John Wiley & Sons. number Publ. 48 in Int. Assoc. Sedimentol. Spec., pp. 543–572. doi:10.1002/9781119424437.ch20.

Willis, B., Tang, H., 2010. Three-dimensional connectivity of point-bar deposits. J. Sediment. Res. 80, 440–454. doi:10.2110/jsr.2010.046.

Wu, C., Bhattacharya, J., Ullah, M., 2015. Paleohydrology and 3d facies architecture of ancient point bars, Ferron Sandstone, Notom Delta, south-central Utah, USA. J. Sediment. Res. 85, 399–418. doi:10.2110/jsr.2015.29.

Yan, N., Colombera, L., Mountney, N., Dorrell, R., 2019. Fluvial point-bar architecture and facies heterogeneity, and their influence on intra-bar static connectivity in humid coastal-plain and dryland fan systems, in: Fluvial Meanders and Their Sedimentary Products in the Rock Record. John Wiley & Sons. number Publ. 48 in Int. Assoc. Sedimentol. Spec., pp. 475–508. doi:10.1002/9781119424437.ch18.

Yang, Y., Lin, X., Elliot, T., Kalin, R., 2001. A natural-gradient field tracer test for evaluation of pollutant-transport parameters in a porous-medium aquifer. Hydrogeol. J. 9, 313–320. doi:10.1007/s100400100127.

Zecchin, M., Baradello, L., Brancolini, G., Donda, F., Rizzetto, F., Tosi, L., 2008. Sequence stratigraphy based on high-resolution seismic profiles in the late pleistocene and holocene deposits of the venice area. Mar. Geol. 253, 185–198. doi:10.1016/j.margeo.2008.05.010.

Zecchin, M., Brancolini, G., Tosi, L., Rizzetto, F., Caffau, M., Baradello, L., 2009. Anatomy of the holocene succession of the southern venice lagoon revealed by very high-resolution seismic data. Cont. Shelf Res. 29, 1343–1359. doi:10.1016/j.csr.2009.03.006.